Nano Energy (2014) 7, 86–96

Available online at www.sciencedirect.com

ScienceDirect

journal homepage: www.elsevier.com/locate/nanoenergy

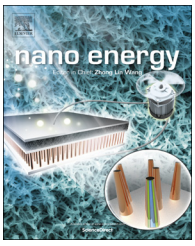

RAPID COMMUNICATION

One-step preparation of single-crystalline Fe_2O_3 particles/graphene composite hydrogels as high performance anode materials for supercapacitors

Huanwen Wang[a], Zijie Xu[a], Huan Yi[a], Huige Wei[b], Zhanhu Guo[b,*], Xuefeng Wang[a,*]

[a]*Department of Chemistry, Key Laboratory of Yangtze River Water Environment, Ministry of Education, Tongji University, Shanghai 200092, China*
[b]*Integrated Composites Laboratory (ICL), Dan F. Smith Department of Chemical Engineering, Lamar University, Beaumont, TX 77710, USA*

Received 30 December 2013; received in revised form 10 March 2014; accepted 16 April 2014
Available online 5 May 2014

KEYWORDS
Graphene;
Fe_2O_3;
Hydrogel;
Anode;
Supercapacitor

Abstract
To increase the energy density of supercapacitors to approach that of batteries, the current research is always directed towards the cathode materials, whereas the anode materials are rarely studied. In the present work, single-crystalline Fe_2O_3 nanoparticles directly grown on graphene hydrogels are investigated as high performance anode materials for supercapacitors. During the formation of the graphene/Fe_2O_3 composite hydrogels, flexible graphene sheets decorated with Fe_2O_3 particles are self-assembled to form interconnected porous microstructures with high specific surface area, which strongly facilitate charge and ion transport in the full electrode. Infrared spectra show that hydrogen bond is formed between C–OH on graphene hydrogels and Fe_2O_3. Benefits from the combined graphene hydrogels and Fe_2O_3 particles in such a unique structure are that the graphene/Fe_2O_3 composite electrode exhibits an ultrahigh specific capacitance of 908 F g^{-1} at 2 A g^{-1} within the potential range from −1.05 to −0.3 V, and an outstanding rate capability (69% capacity retention at 50 A g^{-1}). Furthermore, the cycling performance is clearly much better for the graphene/Fe_2O_3 composite hydrogels than that for pure Fe_2O_3 sample. These findings open a new pathway to the design and fabrication of

*Corresponding authors. Tel.: +86 21 65980301.
E-mail addresses: zhanhu.guo@lamar.edu (Z. Guo), xfwang@tongji.edu.cn (X. Wang).

http://dx.doi.org/10.1016/j.nanoen.2014.04.009

three-dimensional graphene hydrogel composites as anode materials in the development of high-performance energy-storage systems.

Introduction

As a new class of energy storage devices, supercapacitors display the desirable characteristics of high power density (ten times more than batteries), fast rates of charge-discharge (with seconds), excellent cycling stability, and low maintenance cost, which make them one of the most promising candidates for next-generation power devices [1-3]. Unfortunately, the energy storage density of existing supercapacitors is limited, generally one order of magnitude lower than that of batteries [4]. Currently, for practical applications, it is essential to increase the energy density of supercapacitors, without sacrificing the device power density and cycle life. Experimental evidence suggests that electrode materials play a key role in the development of high performance supercapacitors. Among various supercapacitor electrode materials, pseudocapacitive transition-metal oxides and electronically conducting polymers based on faradic redox charge storage have exhibited much higher energy density than that of electrochemical double-layer capacitive carbon materials [5-7]. Different materials have been employed for fabrication of the anode (negative electrode associated with oxidative chemical reactions) and cathode (positive electrode associated reductive chemical reactions) [8]. According to the working potential window in aqueous electrolytes, these pseudocapacitive materials can be divided into two categories: (1) cathode materials (working potential above 0 V vs. SCE), and (2) anode materials (working potential below 0 V vs. SCE). So far, despite great progress having been made in improving the capacitance of cathode materials [8,9], there are only a few reports on anode materials due to the unsatisfactory capacitive performance.

It is noted that carbon-based materials are commonly used as anodes in the asymmetrical supercapacitors because of their high specific surface area, excellent electrical conductivity, and large power density [10,11]. However, the low specific capacitance of carbon materials severely limits the energy density for supercapacitors. Therefore, it is highly desirable to explore new anode materials. It has been reported that metal oxide based anodes such as MoO_{3-x} [12], V_2O_5 [13], TiN [14], VN [15], Bi_2O_3 [16] and FeO_x [17] show much higher energy density than carbon-based materials. Among these anode materials, iron oxides have attracted considerable attention because of their variable oxidation states, natural abundance, low cost, low toxicity and environmental friendliness [18-32]. Particularly, iron oxides possess high hydrogen evolution potential in aqueous solution, thus making them a promising candidate as anode in asymmetrical supercapacitors.

Table 1 summarizes some of the results that have been obtained to date with FeO_x as a supercapacitor electrode material. Except in thin films, the poor electronic conductivity limits the performance of iron oxides in terms of both capacitance and capacitance retention at high current densities. In order to increase electrical conductivity and utilization efficiency, many works have shown supercapacitor application of iron oxides coupled with various carbonaceous materials such as carbon nanotubes, carbon nanofibers, carbon nanosheets, carbon black, carbon foam and graphene. As expected, these FeO_x-carbon composites exhibit enhanced capacitances in comparison with pure iron oxides. For instance, the specific capacitance value of up to 135 F g^{-1} for Fe_3O_4 nanosheets-carbon nanofibers was higher than that of Fe_3O_4 (83 F g^{-1}) [25]. Wu et al. [28] reported the specific capacitance of 510 F g^{-1} for Fe_3O_4, but only under very limiting circumstances: a low oxide weight loading (3 wt%), which resulted in only 40 F g^{-1} normalized to the Fe_3O_4-carbon composite mass. Very recently, 2D sandwich-like Fe_3O_4@graphene nanocomposites showed excellent rate capability, but their specific capacitance was needed to further increase [32]. Therefore, boosting the performance of FeO_x based energy storage by constructing well-defined pathways for efficient ionic and electronic transport remains a major topic of interest.

More recently, self-assembling two-dimensional (2D) graphene sheets into 3D hydrogels opens a new pathway for supercapacitor application [33]. Graphene hydrogels can provide strong mechanical strengths, multidimensional electron transport pathways, easy access to the electrolyte, and minimized transport distances between bulk electrode and electrolyte due to the combination of the 3D interconnected framework and the intriguing properties of graphene [33,34]. The supercapacitors based on graphene hydrogels exhibit ultrahigh rate capability (up to 100 A g^{-1}) and outstanding cycling performance. However, their specific capacitances (128-226 F g^{-1}) are fundamentally limited by the electrical double layer mechanism [35-41]. To enhance energy densities, recent works have shown supercapacitor application of graphene hydrogels combined with some pseudocapacitive cathode materials such as Co_3O_4 [42], $Ni(OH)_2$ [43] and $MnCO_3$ [44]. Besides, graphene/VO_2 composite hydrogels have been reported to exhibit a specific capacitance of 426 F g^{-1} at 1 A g^{-1} in the potential range of -0.6 to 0.6 V, which is indicative of a positive synergistic effect of VO_2 and graphene on the improvement of electrochemical performance [45]. Nevertheless, to the best of our knowledge, a study of iron oxide supported on 3D graphene hydrogels as anode materials for supercapacitors has not been reported to date.

In this paper, a one-step hydrothermal strategy was reported to prepare 3D graphene/Fe_2O_3 composite hydrogels, in which Fe_2O_3 are homogeneously grown on graphene sheets during the formation of graphene hydrogels. Such unique architectures can offer numerous channels for rapid diffusion of electrolyte ions within the electrode material and high electrical conductivity of the overall electrode due to the graphene network. When used as anode materials for supercapacitors, graphene/Fe_2O_3

Table 1 Physical and electrochemical properties reported in recent papers for FeO_x-based electrodes in a negative potential range in various aqueous electrolytes.

FeO_x electrode	Surface area ($m^2\ g^{-1}$)	Electrolyte	Potential range (V vs. SCE)	Specific capacitance ($F\ g^{-1}$)	Rate capability	Ref (year)
Fe_2O_3 nanosheet film	Not reported	1 M Li_2SO_4	−0.9 to −0.1 V	173 at 3 A g^{-1}	117 at 12.3 A g^{-1}	[17] (2009)
Cellular Fe_3O_4 film	Not reported	1 M Na_2SO_4	−0.55 to 0.05 V	105 at 20 mV s^{-1}	Not reported	[18] (2005)
Fe_3O_4 powders	115	0.1 M K_2SO_4	−0.8 to 0.25 V	75 at 10 mV s^{-1}	Not reported	[19] (2003)
Fe_2O_3 film	Not reported	1 M NaOH	−0.6 to 0.1 V	178 at 5 mV s^{-1}	121 at 100 mV s^{-1}	[20] (2011)
Fe_2O_3 nanotube arrays	Not reported	1 M Li_2SO_4	−0.8 to 0 V	138 at 1.3 A g^{-1}	91 at 12.8 A g^{-1}	[21] (2011)
FeOOH rods	Not reported	1 M Li_2SO_4	−0.85 to −0.1 V	116 at 0.5 A g^{-1}	93 at 1.5 A g^{-1}	[22] (2008)
octadecahedron Fe_3O_4 film	Not reported	1 M Na_2SO_3	−1 to 0.1 V	118 at 2 A g^{-1}	50 at 3.3 A g^{-1}	[23] (2009)
Fe_3O_4 nanoparticles	Not reported	1 M Na_2SO_3	−0.9 to 0.1 V	207.7 at 0.4 A g^{-1}	90.4 at 10 A g^{-1}	[24] (2013)
Fe_3O_4/CNF composite	Not reported	1 M Na_2SO_3	−0.9 to 0.1 V	127 at 10 mV s^{-1}	53 at 10 mV s^{-1}	[25] (2011)
Fe_3O_4/CNT composite	Not reported	6 M KOH	−1 to 0 V	129 at 2.5 mA cm^{-1}	103 at 40 mA cm^{-1}	[26] (2013)
Fe_3O_4/carbon nanosheets	229	1 M Na_2SO_3	−0.8 to −0.2 V	163.4 at 1 A g^{-1}	113 at 10 A g^{-1}	[27] (2013)
Fe_3O_4/carbon black	34	1 M Na_2SO_3	−0.75 to 0.5 V	510 for Fe_3O_4 at 15 mA g^{-1}	Not reported	[28] (2003)
Fe_2O_3 nanotube/rGO	Not reported	1 M Na_2SO_4	−1 to 0 V	215 at 2.5 mV s^{-1}	88 at 100 mV s^{-1}	[29] (2012)
FeO_x-carbon nanofoams	431	2.5 M Li_2SO_4	−0.8 to 0.2 V	343 for FeO_x at 5 mV s^{-1}	Not reported	[30] (2010)
Fe_3O_4 particles-graphene	Not reported	1 M KOH	−1 to 0.1 V	220.1 at 0.5 A g^{-1}	134.6 at 5 A g^{-1}	[31] (2014)
FeOOH nanorods/graphene	160	1 M LiOH	−1.15 to 0.1 V	326 at 0.5 A g^{-1}	293 at 10 A g^{-1}	[32] (2011)

composite hydrogels show ultrahigh specific capacitance, outstanding rate capability and enhanced cycling performance.

Experimental section

Synthesis of samples

GO was synthesized from graphite powders by a modified graphite oxide (GO), which was prepared from natural graphite flakes using a modified Hummers method [16,46]. In a typical synthesis process of graphene/Fe_2O_3 composite hydrogels, a 60 mL of GO (2 mg mL^{-1}) aqueous dispersion was mixed with $FeCl_3 \cdot 6H_2O$ (420 mg) by sonication for 4 h. Then the resulting mixture was sealed in a Telfonlined autoclave and was hydrothermally treated at 180 °C for 12 h. Finally, the as-prepared sample was freeze-dried overnight, followed by vacuum drying at 60 °C for 12 h. For comparison, graphene hydrogel and Fe_2O_3 were synthesized by the same procedure in the absence of $FeCl_3 \cdot 6H_2O$ and GO, respectively. The content of Fe_2O_3 was determined by weighing the residue that was obtained after processing the Fe_2O_3/graphene hydrogel composite at 800 °C for 6 h in air atmosphere. The weight percent of Fe_2O_3 in the composite was 65%.

Materials characterization

The products were characterized by field emission scanning electron microscopy (FESEM; Philips XSEM30, Holland), and transmission electron microscope (TEM; JEOL, JEM-2010, Japan). The structure of the samples was examined by X-ray diffraction (XRD; Philips PC-APD) with Cu Kα radiation (λ=1.5418 Å) operating at 40 kV, 60 mA. Raman spectra were collected using a 514 nm laser with RM100 under ambient conditions, with a laser spot size of about 1 mm. Nitrogen adsorption/desorption isotherms were measured at the liquid nitrogen temperature using a Micromeritics Tristar 3000 analyzer. FTIR spectra were recorded at 0.5 cm^{-1}

resolution on a Bruker Vertex 70 V with 0.1 cm^{-1} accuracy using a three-reflection attenuated total reflection (ATR) accessory with a ZnSe internal reflection element (Harrick Scientific Products, Ser No: GATVBR48406071201).

Electrochemical measurement

The working electrodes were prepared by pressing mixtures of the as-prepared powder samples, acetylene black and polytetrafluoroethylene (PTFE) binder (weight ratio of 75:20:5) onto a nickel foam (1×1 cm^2) current collector. The mass of electroactive materials in the working electrode was obtained through weighing bare nickel foam and nickel foam on which the above mixtures were pressed. Each working electrode contained about 1 mg electroactive material and had a geometric surface area of about 1 cm^2. A typical three-electrode experimental cell equipped with a working electrode, a platinum foil counter electrode, and an Hg/HgO reference electrode was used for measuring the electrochemical properties of working electrode. All electrochemical measurements were carried out in 1 M KOH aqueous solution as electrolyte on a CHI660D electrochemical working station.

Results and discussion

Our designed protocol of graphene/Fe_2O_3 composite hydrogels has been shown in Figure 1. Graphene oxide is selected as the substrate for *in situ* growth of Fe_2O_3 particles. Before hydrothermal reduction, the GO sheets are randomly dispersed in water due to their strong hydrophilicity. Subsequently, Fe^{3+} cations from $FeCl_3$ can favorably bind with oxygen-containing groups on GO sheets via electrostatic interactions. At the beginning of hydrothermal reaction, the hydrolysis of Fe^{3+} leads to the formation of FeOOH deposited on the surface of the GO sheets. In the subsequent process, GO becomes regionally hydrophobic because of the diminished oxygenated functionalities and FeOOH is simultaneously decomposed into Fe_2O_3. The uniform decoration of Fe_2O_3 particles on graphene sheets lead to the formation of graphene/Fe_2O_3 hydrogels [33].

The crystal phase and structure information of the products were obtained by XRD measurements. Figure 2 shows the XRD patterns of GO, graphene hydrogels, Fe_2O_3 and graphene/Fe_2O_3 composite hydrogels. The GO pattern is dominated by a single broad peak at 10.3°, which corresponds to an interlayer distance of 8.6 Å (Figure 2a). The expansion of the galleries relative to the graphite (d_{002} = 3.4 Å) is caused by oxidation of the graphene sheets and intercalation of water and oxygen functionalities. The pattern of graphene hydrogels contains a very broad reflection at 23.2° (corresponding to d spacing of 3.7 nm), indicating the formation of a poorly ordered graphite-like material (Figure 2b). Figure 2c and d shows the XRD patterns of Fe_2O_3 and graphene/Fe_2O_3 composite hydrogels, in which all the peaks can be assigned to Fe_2O_3 (JCPDS no. 33-0664). Moreover, no conventional stacking peak (002) of graphene sheets at 2θ=23.2° is detected, suggesting that the residual graphene sheets may be individual monolayers that are homogeneously dispersed in the resultant 3D framework.

Raman spectroscopy can be used to gain information about the structure of the samples. The Raman spectra of GO, graphene hydrogels, Fe_2O_3 and graphene/Fe_2O_3 composite hydrogels are shown in Figure 3. From the relative intensities of the D and G band peaks at 1350 and 1581 cm^{-1} (Figure 3a, b), it can be concluded that the conjugated G network (sp^2 carbon) will be re-established during hydrothermal reduction of GO. As can be seen in Figure 3c, the fundamental Raman scattering peaks for Fe_2O_3 are observed at 218, 277, 389, 486, and 595 cm^{-1} corresponding to the $A_{g1}(1)$, $E_{g2}+E_{g3}$, E_{g4}, $A_{1g}(2)$, E_{g5} modes [29], respectively.

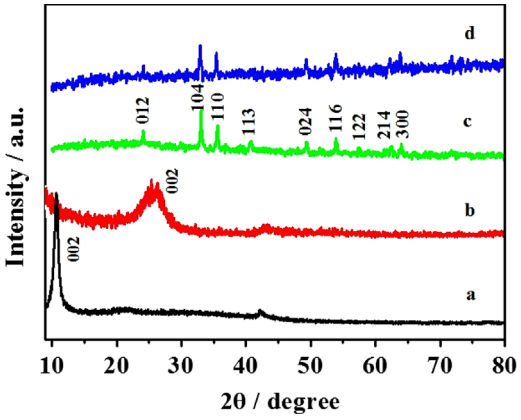

Figure 2 XRD patterns of (a) GO, (b) graphene hydrogels, (c) Fe_2O_3 and (d) graphene/Fe_2O_3 composite hydrogels.

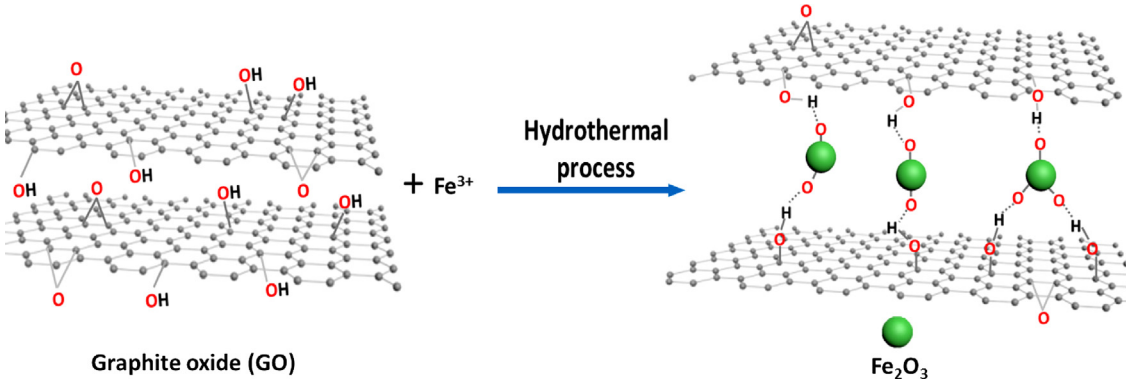

Figure 1 The formation process of 3D graphene/Fe_2O_3 composite hydrogels.

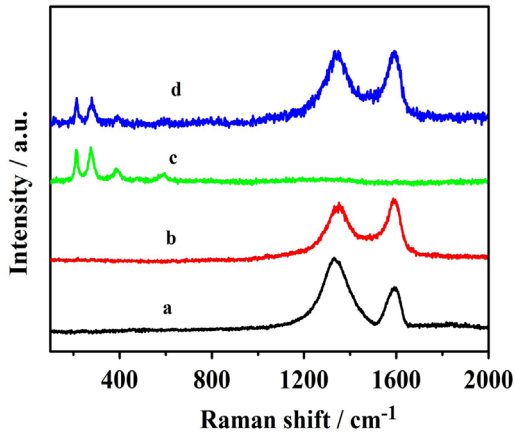

Figure 3 Raman spectra of (a) GO, (b) graphene hydrogels, (c) Fe_2O_3 and (d) graphene/Fe_2O_3 composite hydrogels.

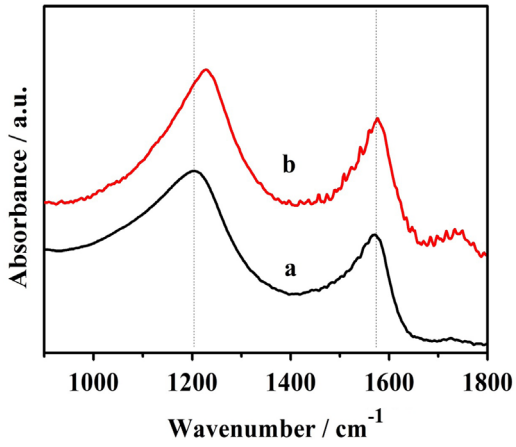

Figure 4 ATR-FTIR spectra of (a) graphene hydrogels and (b) graphene/Fe_2O_3 composite hydrogels.

For the graphene/Fe_2O_3 composite hydrogels (Figure 3d), in addition to the bands corresponding to Fe_2O_3, the characteristic D and G bands of graphene also appear clearly, respectively. These results further suggest the good integration of graphene and Fe_2O_3 nanoparticles.

To reveal the interaction between Fe_2O_3 nanoparticles and graphene in the composite hydrogel, ATR-FTIR measurements are carried out. Figure 4 shows ATR-FTIR spectra of graphene hydrogels and graphene/Fe_2O_3 composite hydrogels. For the graphene hydrogels (Figure 4a), the bands appearing at 1208 and 1572 cm^{-1} are attributed to the C–O (H) stretching peak and the skeletal vibration of the graphene sheets, respectively [4]. For the composite hydrogels, the characteristic absorption peak of graphene at about 1572 cm^{-1} is clearly observed in Figure 4b, which is consistent with pure graphene hydrogels. However, the C–O (H) stretching peak (1229 cm^{-1}) for graphene/Fe_2O_3 composite hydrogels shows an obvious blue-shift in comparison with graphene hydrogels (1208 cm^{-1}). This phenomenon implies the existence of intramolecular hydrogen bonding. When the hydrogen (H) in C–OH is bound to the highly electronegative oxygen (O) in Fe_2O_3, the interaction between carbon (C) in graphene and oxygen (O) in OH group will become stronger, resulting in blue-shift of C–O (H) stretching vibration. This formation of the hydrogen bonding between C–OH in graphene and Fe_2O_3 is beneficial to mitigating polarization of the electrode or enhancing utilization of the active materials [6].

The nitrogen adsorption and desorption isotherms of the as-prepared graphene hydrogels and graphene/Fe_2O_3 composite hydrogels exhibit type IV characteristics (Figure 5a and b), which are indicative of the presence of relatively

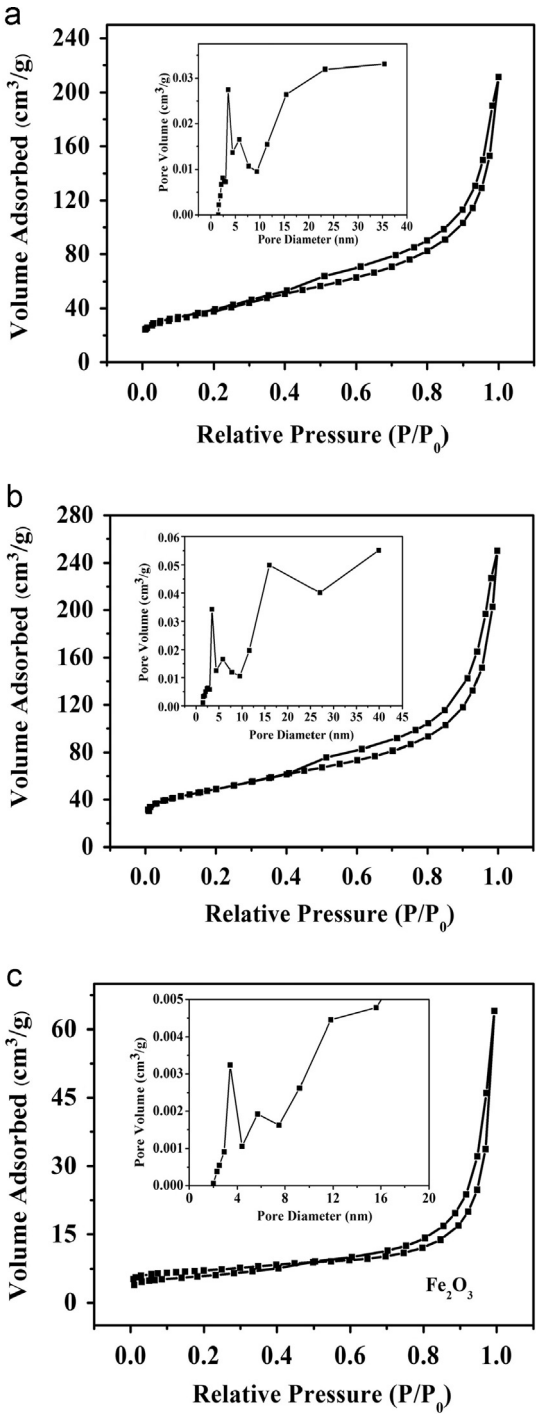

Figure 5 Nitrogen adsorption and desorption isotherms measured at 77 K for (a) graphene hydrogels, (b) graphene/Fe_2O_3 composite hydrogels and (c) Fe_2O_3. The insets show the corresponding BJH pore size distributions.

large pores in the samples. For pure Fe_2O_3 sample (Figure 5c), a small step of N_2 adsorption and desorption branches occurs at the relative high pressure (P/P_0), indicating that the pores mainly comes from the voids among the nanoparticles. It is worth noting that the Brunauer–Emmett–Teller (BET) specific surface area of graphene/Fe_2O_3 composite hydrogels (173 $m^2 g^{-1}$) is much higher than that of graphene hydrogels (134 $m^2 g^{-1}$) and of pure Fe_2O_3 powder (24 $m^2 g^{-1}$). This result strongly suggests that the Fe_2O_3 particles anchored on the separated graphene surface prevent the graphene sheets from aggregating and restacking [47], as illustrated in Figure 1. The large specific surface areas will undoubtedly shorten the ion diffusion paths and enhance the utilization of active materials, which can contribute to an improved pseudocapacitive performance. The pore size distribution of the sample calculated by desorption isotherm using Barret–Joyner–Halenda (BJH) method is shown in inset of Figure 5. The as-prepared graphene hydrogels and graphene/Fe_2O_3 composite hydrogels have similar pore-size distributions, from micropores to macropores. Importantly, an apparent increment in pore volume is observed from 0.327 $cm^3 g^{-1}$ for graphene hydrogels to 0.387 $m^3 g^{-1}$ for graphene/Fe_2O_3 composite hydrogels, further indicating the separation of graphene sheets induced by the loading of Fe_2O_3 particles. For comparison, pore volume of pure Fe_2O_3 nanoparticles is

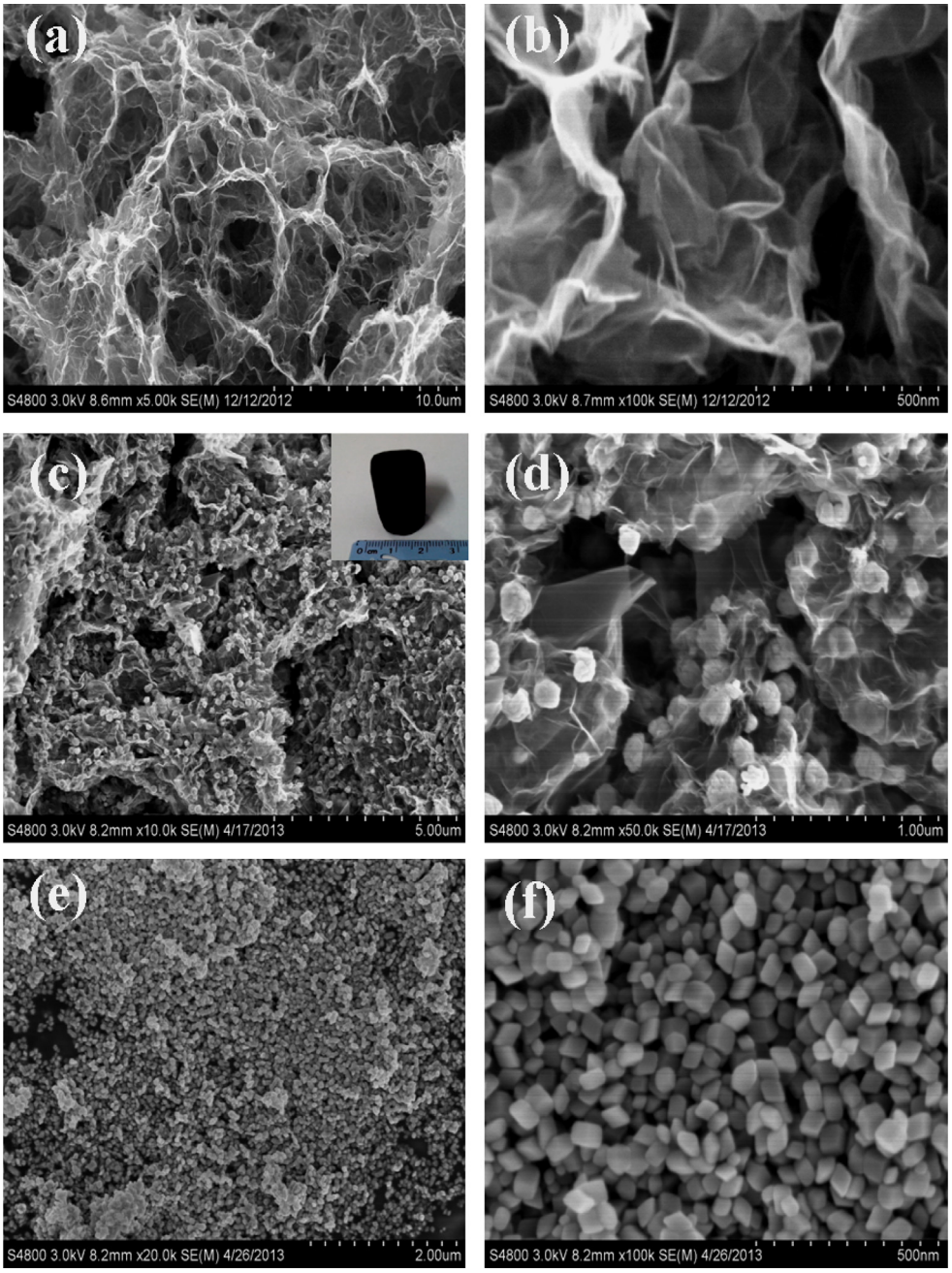

Figure 6 FESEM images of (a, b) graphene hydrogels, (c, d) graphene/Fe_2O_3 composite hydrogels and (e, f) Fe_2O_3. The inset shows the photograph of graphene/Fe_2O_3 composite hydrogels.

only 0.098 $cm^3\ g^{-1}$, which confirms the dispersion interaction of graphene hydrogels with Fe_2O_3 particles.

The surface morphologies of the as-synthesized samples are imaged by FESEM. Graphene hydrogels have a macroporous morphology with the framework network (Figure 6a). The ultrathin and flexible nature of graphene sheets can be clearly observed in high magnification FESEM image (Figure 6b). Low magnification FESEM image of graphene/Fe_2O_3 composite hydrogels clearly shows that the Fe_2O_3 particles are anchored uniformly on both sides of the graphene sheets (Figure 6c). From high magnification FESEM image (Figure 6d), we can find that some Fe_2O_3 particles with a size of 50–200 nm have been encapsulated within the graphene sheets, which can efficiently prevent the aggregation of Fe_2O_3 particles. This result also reveals graphene hydrogel as an interconnected 3D network structure with dispersed pores of several micrometers in diameter, suggesting efficient assembly between the particles and graphene sheets during the hydrothermal treatment. Such composite framework could enhance the interface contact and suppress the dissolution and agglomeration of particles, thereby promoting the electrochemical activity and stability of the graphene/Fe_2O_3 composite. For comparison, pure Fe_2O_3 sample is synthesized by the same procedure in the absence of GO. As shown in Figure 6e and f, the as-prepared Fe_2O_3 nanoparticles exhibit uniform cube-shaped structures with the edge length of 50–100 nm. This morphology difference reveals that the strong interaction between GO sheets and Fe^{3+} have an important effect on the crystal growth of Fe_2O_3 nanocrystals.

To characterize further the microstructure of the graphene/Fe_2O_3 composite hydrogels, TEM studies are carried

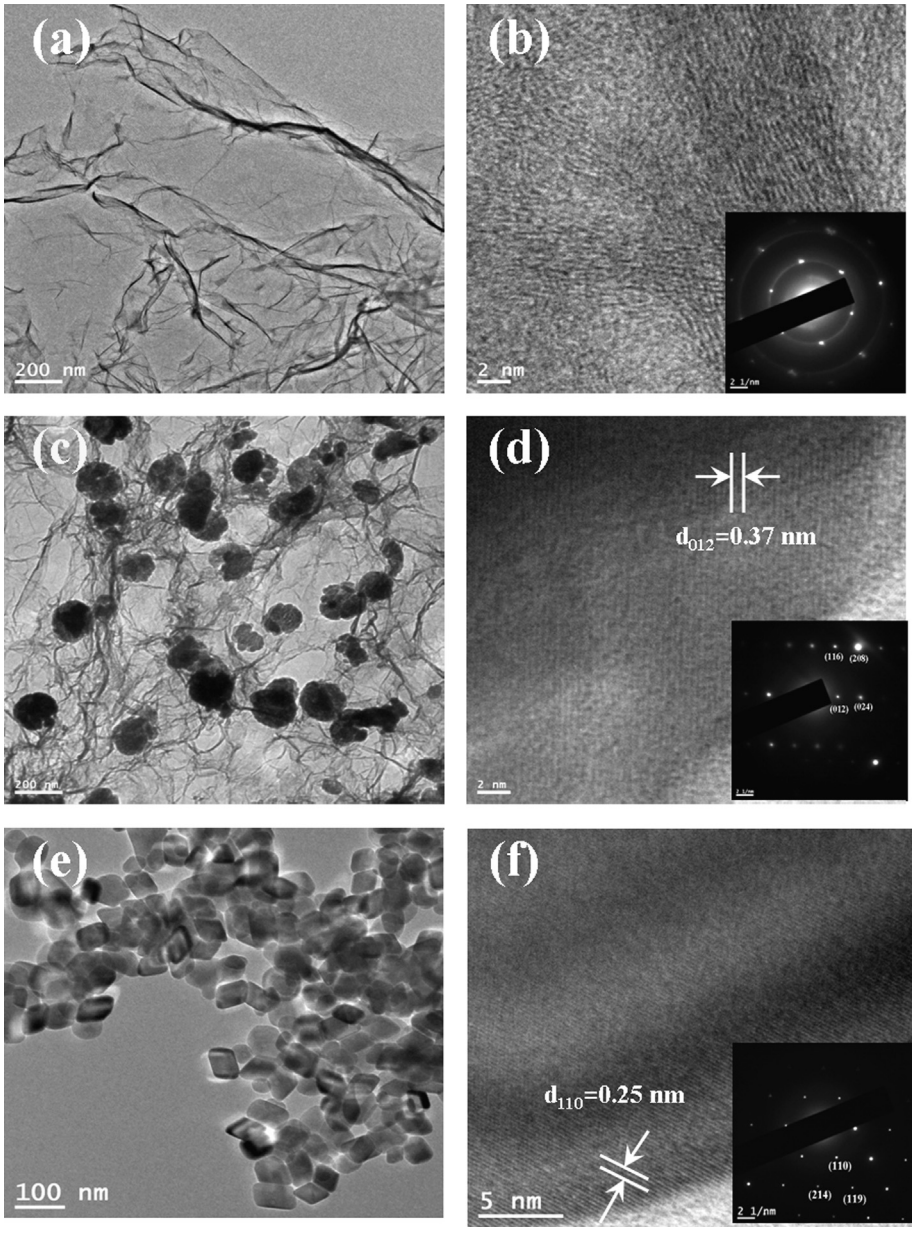

Figure 7 TEM images of (a, b) graphene hydrogels, (c, d) graphene/Fe_2O_3 composite hydrogels and (e, f) Fe_2O_3. The insets show the corresponding SAED pattern.

out (Figure 7). For comparison, we also present the TEM images of graphene hydrogels and the Fe_2O_3 sample. Figure 7a shows that graphene layers from hydrogels are almost transparent with some wrinkles visible under TEM. High-resolution TEM (HRTEM) and selected-area electron diffraction (SAED) patterns (Figure 7b) further support the production of individual high-quality crystalline graphene sheets. For the composite hydrogel material (Figure 7c), a sheet-like shape of graphene is uniformly deposited with numerous nanoparticles. The HRTEM image of graphene/Fe_2O_3 composite hydrogels reveals typical regular lattice fringes with the d spacing of 0.37 nm, corresponding to the (012) plane of Fe_2O_3 (Figure 7d). More interestingly, the SAED pattern (inset of Figure 7d) demonstrates the single crystalline structure of the Fe_2O_3. The reflection spots in SAED of Figure 7d recorded from the particles in Figure 7c can be indexed to the Fe_2O_3 crystal structure (JCPDS no. 33-0664). For pure Fe_2O_3, uniform cube shape is clearly observed in Figure 7e. From the HRTEM image (Figure 7f), the lattice fringes with a spacing of 0.58 nm is in good agreement with the spacing of the (110) plane of Fe_2O_3. Single crystalline structure is also confirmed by the (SAED) pattern (inset of Figure 7f). The different crystal orientation of HRTEM images would decide the morphology difference of Fe_2O_3, as observed in Figure 6d and f.

To evaluate the properties of the prepared samples as supercapacitor electrodes, we perform cyclic voltammetry (CV) and galvanostatic charge–discharge measurements. Figure 8a shows the typical CV curves of graphene hydrogels, Fe_2O_3 and graphene/Fe_2O_3 composite hydrogels within the potential range from −1.2 to −0.3 V at a scan rate of 10 mV s^{-1}. When the potential is below the −1 V, hydrogen evolution phenomenon becomes obvious for the graphene hydrogels (inset of Figure 8a). In the potential range from −1 to −0.3 V (Figure 8b), the CV curves of graphene hydrogels exhibit typical rectangular shape at different sweep rates, indicative of good charge propagation at the electrode surface following the electric double layer charging mechanism. As shown in Figure 8a, the CV curve of graphene/Fe_2O_3 composite hydrogels has one pair of redox peaks, corresponding to conversion between Fe^{2+} and Fe^{3+} [32,48]. When scanned to the more negative potential direction, Fe^{3+} is reduced to Fe^{2+} before appreciable hydrogen evolution (Figure 8a). Meanwhile, Fe^{2+} is oxidized to Fe^{3+} when scanned to the positive direction, consistent with the single oxidation peak observed in CV. The CV curves of graphene/Fe_2O_3 composite hydrogels retain a similar shape even at high scan rate, indicating an excellent capacitance behavior and fast diffusion of the electrolyte ions into the composite electrode (Figure 8d). From Figure 8a, the CV curve of the Fe_2O_3 sample is similar to that of graphene/Fe_2O_3 composite hydrogels. However, the area under the CV curves is clearly much larger for the graphene/Fe_2O_3 composite hydrogels than that for the

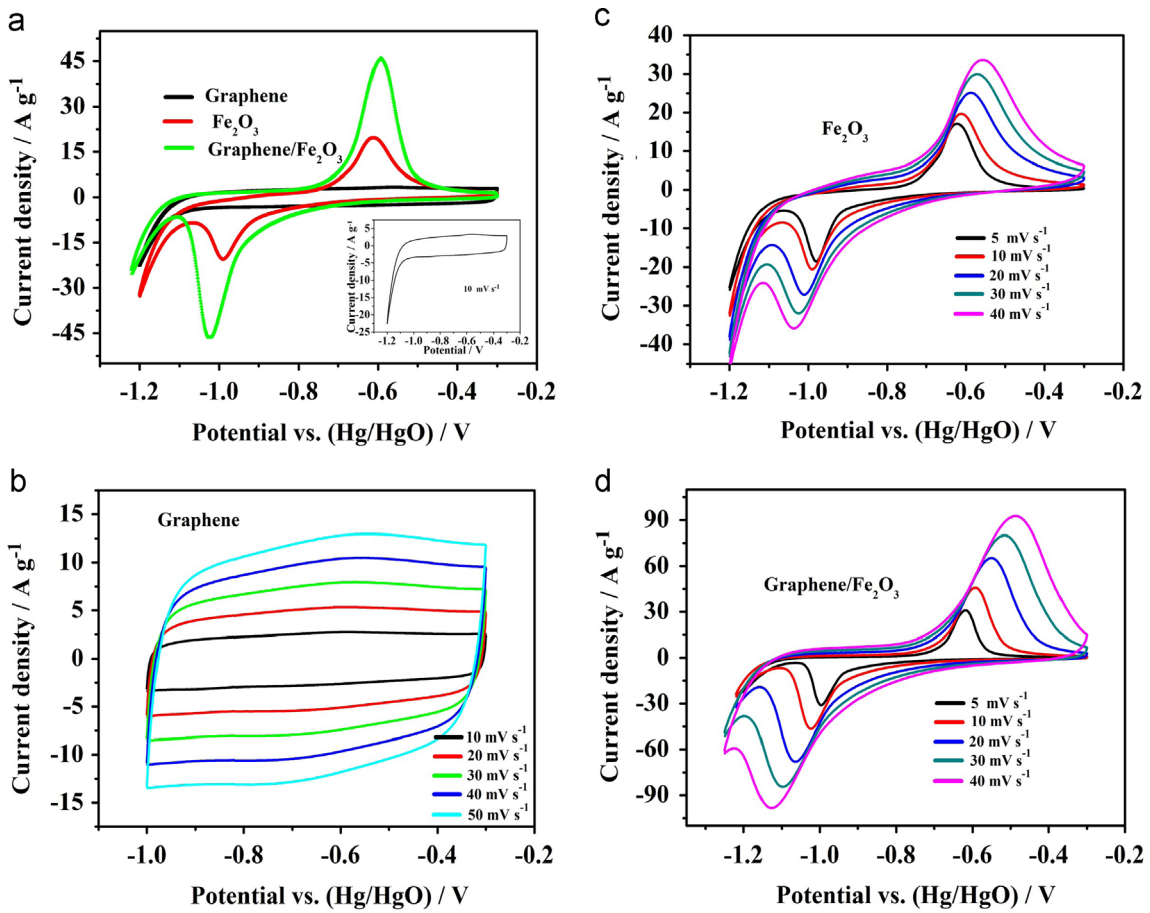

Figure 8 CV curves of (a) the samples at 5 mV s^{-1}, (b) graphene hydrogels, (c) Fe_2O_3 and (d) graphene/Fe_2O_3 composite hydrogels at different sweep rates. The insets show the CV curve of graphene hydrogels at 10 mV s^{-1}.

Fe_2O_3 at the same scan rate (Figure 8c, d). It is well-known that the specific capacitance is proportional to the area of the CV curve (Figure 8c, d) [6,49]. This indicates that the graphene/Fe_2O_3 composite hydrogels have clearly higher capacitances than that of the Fe_2O_3.

Galvanostatic charge−discharge is a reliable method for measuring the specific capacitance of supercapacitors at constant currents. Figure 9a, b and c shows galvanostatic charge−discharge curves of graphene hydrogels, Fe_2O_3 and graphene/Fe_2O_3 composite hydrogels at different current densities. The specific potential window of −1.05 and −0.3 V is adopted to avoid the hydrogen-evolution reaction. The increase in the discharging time represents a higher capacitance of the graphene/Fe_2O_3 composite hydrogels. The specific capacitance is calculated by $I\Delta t/m\Delta V$, where I is the constant discharge current, Δt is the discharging time, m is the mass of active material in a single electrode, and ΔV is the voltage drop upon discharging. According to the discharging curves, the relationship between specific capacitance and current density is illustrated in Figure 9d. Graphene hydrogels exhibit a capacitance of 272 F g^{-1} at 2 A g^{-1} with the capacitance retention of 55% at 50 A g^{-1}, which is mainly ascribed to the electric double-layer capacitance. For the graphene/Fe_2O_3 electrode, the combination of electric double-layer capacitance and faradaic capacitance is responsible for the longer discharge duration due to faradaic charge-transfer accompanied by the double-layer charging process. The capacitance value of graphene/Fe_2O_3 composite hydrogels is as high as 908 F g^{-1} at 2 A g^{-1}. Even at the high current density of 50 A g^{-1}, the specific capacitance value of the composite is still up to 622 F g^{-1}. To the best of our knowledge, such high specific capacitance and excellent rate capability are superior to the best results reported for FeO_x-based supercapacitor electrodes in the literature (Table 1). In contrast, Fe_2O_3 delivers a much lower capacitance value of 91 F g^{-1} at 20 A g^{-1},with only 10% retention in comparison with 2 A g^{-1}. The clearly improved capacitive performance may be attributed to the rational combination of graphene and Fe_2O_3 into the integrated hydrogel architecture. Due to the high specific capacitance, wide working potential range and high capacitance retention at high current density, the graphene/Fe_2O_3 composite hydrogels are potential to provide very high energy and power density by coupling with a suitable cathode material with a high oxygen evolution potential (such as MnO_2 [50], $Ni(OH)_2$ [51], $NiCo_2O_4$ [1], etc).

Because a long cycling performance is among the most important criteria for supercapacitors, an endurance test is conducted at 20 mV s^{-1} (Figure 10). The first five CV curves of Fe_2O_3 and graphene/Fe_2O_3 composite hydrogels are shown in the inset of Figure 10a and b, respectively. It can be seen that the area reduction of the CV curves with the cycling number is much faster for the Fe_2O_3 sample than

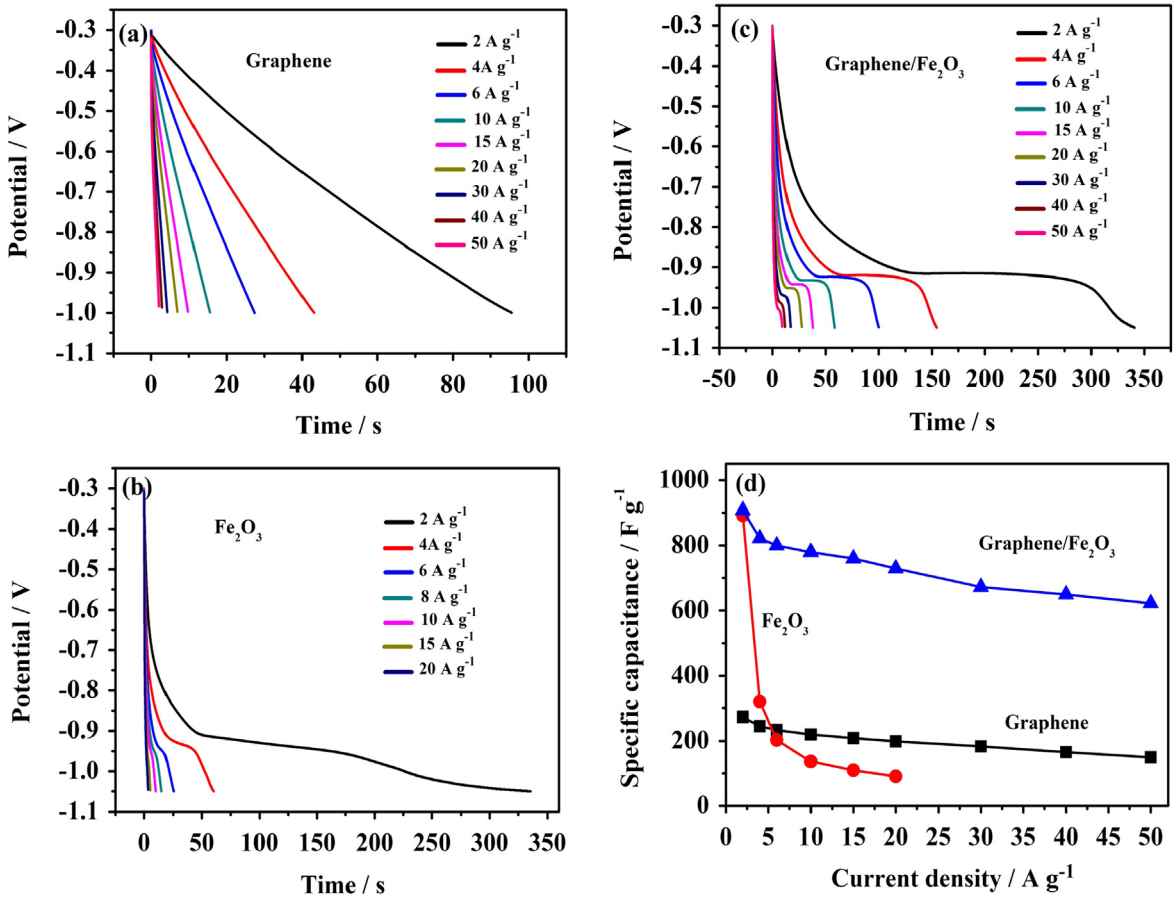

Figure 9 Galvanostatic charge-discharge curves of (a) graphene hydrogels, (b) Fe_2O_3 and (c) graphene/Fe_2O_3 composite hydrogels at different current densities; (d) capacitances versus current densities.

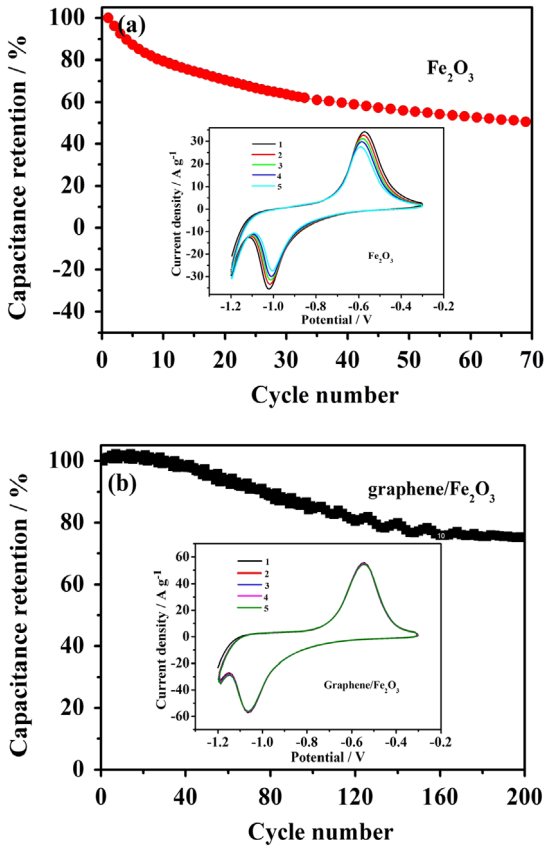

Figure 10 Cycling performance of (a) Fe_2O_3 and (b) graphene/Fe_2O_3 composite hydrogels at 20 mV s^{-1}. The inset in Figure 9 is the first five CV curves.

for the graphene/Fe_2O_3 composite hydrogels. For the Fe_2O_3 sample, the capacitance loss after a 70-cycle test is up to 51% (Figure 10a). This obvious decay in specific capacitance may be caused by the mechanical expansion of Fe_2O_3 during ion insertion/desertion process, Fe_2O_3 detachment from electrode surfaces and Fe dissolution into electrolyte [30]. When Fe_2O_3 particles are encapsulated within the graphene hydrogels, cycling performance of Fe_2O_3 is clearly enhanced. For graphene/Fe_2O_3 composite hydrogels (Figure 10b), 75% of the initial capacitance can be maintained after 200 cycles. This result strongly indicates that the integration of Fe_2O_3 particles in the 3D graphene hydrogels can (1) reduce the chemical dissolution of iron in the cycling process by providing an electrolyte buffer and (2) serve as a matrix to maintain the iron oxide microstructure.

Conclusions

We have successfully prepared graphene/Fe_2O_3 composite hydrogels through a scalable one-step method by using commercial $FeCl_3 \cdot 6H_2O$ and graphene oxide as precursors. In the hybrid architecture, Fe_2O_3 nanoparticles are anchored uniformly on the flexible graphene sheets, forming a porous network framework with hydrogen bond between C–OH on graphene hydrogels and Fe_2O_3. Because of fast ionic and electronic transport, graphene/Fe_2O_3 composite hydrogels provide tremendous potential for energy storage applications. When used as anode materials of supercapacitors, these graphene/Fe_2O_3 composite hydrogels exhibit ultrahigh specific capacitance, remarkable rate capability and enhanced cycling ability. The excellent electrochemical performance of graphene/Fe_2O_3 composite hydrogels originates from the synergistic effect of graphene hydrogels and Fe_2O_3 particles, and the hierarchical microstructure of the hybrid hydrogels. Furthermore, the electrode structure and fabrication method described in this study is simple and should thus be readily applicable to other applications such as electrode materials for Li/Na-ion batteries, electrocatalysts for oxygen evolution, electrosynthesis and so on.

Acknowledgments

This work was supported by the National Natural Science Foundation of China (Nos. 21173158 and 21373152).

References

[1] T.Y. Wei, C.H. Chen, H.C. Chien, S.Y. Lu, C.C. Hu, Adv. Mater. 22 (2010) 347–351.
[2] M.D. StollerR.S. Ruoff, Energy Environ. Sci. 3 (2010) 1294–1301.
[3] X. Xia, J. Tu, Y. Zhang, J. Chen, X. Wang, C. Gu, C. Guan, J. Luo, H.J. Fan, Chem. Mater. 24 (2012) 3793–3799.
[4] H.W. Wang, Z.A. Hu, Y.Q. Chang, Y.L. Chen, H.Y. Wu, Z.Y. Zhang, Y.Y. Yang, J. Mater. Chem. 21 (2011) 10504–10511.
[5] C. Guan, X. Li, Z. Wang, X. Cao, C. Soci, H. Zhang, H.J. Fan, Adv. Mater. 24 (2012) 4186–4190.
[6] Z.A. Hu, Y.L. Xie, Y.X. Wang, L.J. Xie, G.R. Fu, X.Q. Jin, Z.Y. Zhang, Y.Y. Yang, H.Y. Wu, J. Phys. Chem. C 113 (2009) 12502–12508.
[7] Y. Zhai, Y. Dou, D. Zhao, P.F. Fulvio, R.T. Mayes, S. Dai, Adv. Mater. 23 (2011) 4828–4850.
[8] L.L. Zhang, X.S. Zhao, Chem. Soc. Rev. 38 (2009) 2520–2531.
[9] G. Yu, X. Xie, L. Pan, Z. Bao, Y. Cui, Nano Energy 2 (2013) 213–234.
[10] H. Wang, Y. Wang, Z. Hu, X. Wang, ACS Appl. Mater. Interfaces 4 (2012) 6827–6834.
[11] Z. Fan, J. Yan, L. Zhi, Q. Zhang, T. Wei, J. Feng, M. Zhang, W. Qian, F. Wei, Adv. Mater. 22 (2010) 3723–3728.
[12] W. Tang, L. Liu, S. Tian, L. Li, Y. Yue, Y. Wu, K. Zhu, Chem. Commun. 47 (2011) 10058–10060.
[13] Q. Qu, Y. Zhu, X. Gao, Y. Wu, Adv. Energy Mater 2 (2012) 950–955.
[14] X. Lu, G. Wang, T. Zhai, M. Yu, S. Xie, Y. Ling, C. Liang, Y. Tong, Y. Li, Nano Lett. 12 (2012) 5376–5381.
[15] D. Choi, G.E. Blomgren, P.N. Kumta, Adv. Mater. 18 (2006) 1178–1182.
[16] H.W. Wang, Z.A. Hu, Y.Q. Chang, Y.L. Chen, Z.Q. Lei, Z.Y. Zhang, Y.Y. Yang, Electrochim. Acta 55 (2010) 8974–8980.
[17] M.S. Wu, R.H. Lee, J.J. Jow, W.D. Yang, C.Y. Hsieh, B.J. Weng, Electrochem. Solid-State Lett. 12 (2009) A1–A4.
[18] K.W. Chung, K.B. Kim, S.H. Han, H. Lee, Electrochem. Solid-State Lett. 8 (2005) A259–A262.
[19] T. Brousse, D. Bélanger, Electrochem. Solid-State Lett. 6 (2003) A244–A248.
[20] P.M. Kulal, D.P. Dubal, C.D. Lokhande, V.J. Fulari, J. Alloys Compd. 50 (2011) 2567–2571.
[21] K. Xie, J. Li, Y. Lai, W. Lu, Z. Zhang, Y. Liu, L. Zhou, H. Huang, Electrochem. Commun. 13 (2011) 657–660.
[22] W.H. Jin, G.T. Cao, J.Y. Sun, J. Power Sources 175 (2008) 686–691.

[23] J. Chen, K. Huang, S. Liu, Electrochim. Acta 55 (2009) 1-5.
[24] L. Wang, H. Ji, S. Wang, L. Kong, X. Jiang, G. Yang, Nanoscale 5 (2013) 3793-3799.
[25] J. Mu, B. Chen, Z. Guo, M. Zhang, Z. Zhang, P. Zhang, C. Shao, Y. Liu, Nanoscale 3 (2011) 5034-5040.
[26] D. Guan, Z. Gao, W. Yang, J. Wang, Y. Yuan, B. Wang, M. Zhang, L. Liu, Mater. Sci. Eng. B 178 (2013) 736-743.
[27] D. Liu, X. Wang, X. Wang, W. Tian, J. Liu, C. Zhi, D. He, Y. Bandoa, D. Golberg, J. Mater. Chem. A 1 (2013) 1952-1955.
[28] N.L. Wu, S.Y. Wang, C.Y. Han, D.S. Wu, L.S. Shiue, J. Power Sources 113 (2003) 173-178.
[29] K.K. Lee, S. Deng, H.M. Fan, S. Mhaisalkar, H.R. Tan, E.S. Tok, K.P. Loh, W.S. Chin, C.H. Sow, Nanoscale 4 (2012) 2958-2961.
[30] M.B. Sassin, A.N. Mansour, K.A. Pettigrew, D.R. Rolison, J. W. Long, ACS Nano 4 (2010) 4505-4514.
[31] Q. Wang, L. Jiao, H. Du, Y. Wang, H. Yuan, J. Power Sources 245 (2014) 101-106.
[32] Q. Qu, S. Yang, X. Feng, Adv. Mater. 23 (2011) 5574-5580.
[33] Y. Xu, K. Sheng, C. Li, G. Shi, ACS Nano 4 (2010) 4324-4330.
[34] Z.S. Wu, Y. Sun, Y.Z. Tan, S. Yang, X. Feng, K. Müllen, J. Am. Chem. Soc. 134 (2012) 19532-19535.
[35] Y. Xu, Z. Lin, X. Huang, Y. Liu, Y. Huang, X. Duan, ACS Nano 7 (2013) 4042-4049.
[36] K.X. Sheng, Y.Q. Sun, C. Li, W.J. Yuan, G.Q. Shi, Sci. Rep. 2 (2012) 247.
[37] Z.S. Wu, A. Winter, L. Chen, Y. Sun, A. Turchanin, X. Feng, K. Müllen, Adv. Mater. 24 (2012) 5130-5135.
[38] X. Zhang, Z. Sui, B. Xu, S. Yue, Y. Luo, W. Zhan, B. Liu, J. Mater. Chem. 21 (2011) 6494-6497.
[39] L. Zhang, G.Q. Shi, J. Phys. Chem. C 115 (2011) 17206-17212.
[40] J. Chen, K.X. Sheng, P.H. Luo, C. Li, G.Q. Shi, Adv. Mater. 24 (2012) 4569-4573.
[41] W.F. Chen, L.F. Yan, Nanoscale 3 (2011) 3132-3137.
[42] J. Yuan, J. Zhu, H. Bi, X. Meng, S. Liang, L. Zhang, X. Wang, Phys. Chem. Chem. Phys. 15 (2013) 12940-12945.
[43] S. Chen, J. Duan, Y. Tang, S.Z. Qiao, Chem. Eur. J. 19 (2013) 7118-7124.
[44] J. Yuan, J. Zhu, H. Bi, Z. Zhang, S. Chen, S. Liang, X. Wang, RSC Adv. 3 (2013) 4400-4407.
[45] H. Wang, H. Yi, X. Chen, X Wang, J. Mater. Chem. A 2 (2014) 1165.
[46] W.S. Hummers, R.E Offeman, J. Am. Chem. Soc. 80 (1958) 1339.
[47] Y.C. Si, E.T. Samulski, Chem. Mater. 20 (2008) 6792-6797.
[48] B.T. Hanga, T. Watanabe, M. Eashira, S. Okada, J.i. Yamaki, S. Hata, S.H. Yoon, I. Mochida, J. Power Sources 150 (2005) 261-271.
[49] J.W. Lee, A.S. Hall, J.D. Kim, T.E. Mallouk, Chem. Mater. 24 (2012) 1158-1164.
[50] W. Wei, X. Cui, W. Chen, D.G. Ivey, Chem. Soc. Rev. 40 (2011) 1697-1721.
[51] H. Wang, H.S. Casalongue, Y. Liang, H. Dai, J. Am. Chem. Soc. 132 (2010) 7472-7477.

Huanwen Wang received a B.S. degree from the Northwest Normal University in 2008. Now he is a Ph.D. candidate under the supervision of Prof. Xuefeng Wang from Tongji University. His research interest is focused on materials synthesis for energy storage and conversion.

Dr. Zijie Xu is currently Associate Professor at the Department of Chemistry of Tongji University. He received a Ph.D. degree in University of Science and Technology of China in 2002, and then worked as a postdoc fellow in 2002-2004 at Technical Institute of Physics and Chemistry in Chinese Academy of Sciences. His recent research is focused on carbon materials development for energy storage.

Huan Yi received his B.S. degree in 2011 from Northeast Normal University, China. He is currently pursuing his Ph.D. under the supervision of Prof. Xuefeng Wang at Tongji University. His research focuses on design and synthesis of advanced functional materials for energy applications.

Huige Wei, currently a Ph.D. candidate in Dan F Smith Department of Chemical Engineering at Lamar University, obtained both her M.S. (2011) and B.E. (2009) degrees from the Department of Chemical Engineering and Technology at Harbin Institute of Technology, Harbin, China. Currently, her research interests mainly focus on polymer based nanocomposites for electrochromic, energy storage, and anticorrosion applications.

Dr. Zhanhu Guo is currently an Associate Professor of Chemical Engineering at the Lamar University, obtained a Chemical Engineering Ph.D. degree from Louisiana State University (2005) and received three-year (2005-2008) postdoctoral training in Mechanical and Aerospace Engineering Department in University of California Los Angeles. Dr. Guo, chair of the Composite Division of American Institute of Chemical Engineers (AIChE, 2010-2011), directs the Integrated Composites Laboratory (ICL) with more than 20 members. Currently, Dr. Guo's research team focuses on fundamental science of multifunctional nanocomposites for energy, electronic devices, environmental remediation, electromagnetic radiation shielding/absorption, anti-corrosion, fire-retardancy, and sustainability applications.

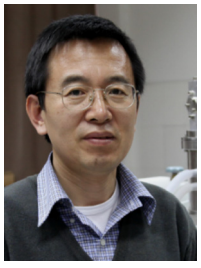

Dr. Xuefeng Wang is a distinguished professor at the Department of Chemistry in Tongji University. Before joining Tongji University in 2009 he was a senior scientist at the Department of Chemistry University of Virginia. He received a B.S. degree from the Northwest Normal University in 1983 and Ph.D. from Fudan University in 1996. Dr. Wang's research interests include metal reactions with hydrogen, designing particles in composites and related advanced materials, and their potential applications in energy storage.